SCIENTIFIC REPORTS

OPEN

SUBJECT AREAS:
SOLID-STATE LASERS
MICRORESONATORS

Received
10 July 2014

Accepted
13 October 2014

Published
12 November 2014

Correspondence and requests for materials should be addressed to H.B.F. (hongbing.fu@iccas.ac.cn)

Shape-Engineering of Self-Assembled Organic Single Microcrystal as Optical Microresonator for laser Applications

Xuedong Wang[1,2], Qing Liao[3], Xiaomei Lu[3], Hui Li[1,2], Zhenzhen Xu[3] & Hongbing Fu[1,3]

[1]Beijing National Laboratory for Molecular Sciences (BNLMS), Institute of chemistry, Chinese Academy of Sciences, Beijing, 100190, P. R. China, [2]Graduate University of Chinese Academy of Sciences, Beijing 100049, P. R. China, [3]Beijing Key Laboratory for Optical Materials and Photonic Devices, Department of Chemistry, Capital Normal University, Beijing 100048, P. R. China.

Single micro/nanocrystals based on π-conjugated organic molecules have caused tremendous interests in the optoelectronic applications in laser, optical waveguide, nonlinear optics, and field effect transistors. However, the controlled synthesis of these organic micro/nanocrystals with regular shapes is very difficult to achieve, because the weak interaction (van der Waals' force, *ca.* 5 kJ/mol) between organic molecules could not dominate the kinetic process of crystal growth. Herein, we develop an elaborate strategy, selective adhesion to organic crystal plane by the hydrogen-bonding interaction (*ca.* 40 kJ/mol), for modulating the kinetic process of the formation of microcrystal, which leads to the self-assembly of one organic molecule 3-[4-(dimethylamino)phenyl]-1-(2-hy-droxyphenyl)prop-2-en-1-on (HDMAC) into one-dimensional (1D) microwires and 2D microdisks respectively. Furthermore, these as-prepared microcrystals demonstrate shape-dependent microresonator properties that 1D microwires act as Fabry-Pérot (FP) mode lasing resonator and 2D microdisks provide the whispering-gallery-mode (WGM) resonator for lasing oscillator. More significantly, through the investigation of the size-effect on the laser performance, single-mode lasing at red wavelength was successfully achieved in the self-assembled 2D organic microdisk at room temperature. These easily fabricated organic single-crystalline microcrystals with controlled shapes are the natural laser sources, which offer considerable promise for the multi-functionalities of coherent light devices integrated on the optics microchip.

Micro- and nanostructures of materials have impressive footprint on the continued development of materials science[1–9]. The shape and the size of these micro/nanostructures precisely lie at the heart of the physical and chemical properties of the functional micro/nanomaterials[10–16]. In recent decades, tremendous efforts have been made towards the development of synthetic procedures for inorganic compounds, such as Ag, Pd, and ZnO[17–19]. The Ag nanocrystals with controlled shape contributes to a distinguished discovery of shape- and size-dependent plasmon resonance[20–22]. More significantly, EI-Sayed M. A. and coworkers demonstrated that Pt nanoparticles of different shapes have different facets, which could be the reason causes different catalytic activities for the same chemical reaction[23]. As compared with inorganic counterparts, organic materials exhibit several inherent advantages, such as compatibility with plastic substrates, tunable optical properties, amenability to low-cost, and low-temperature processing[24]. Thus in recent years, organic single micro/nanocrystals has witnessed prosperous progress in the organic optoelectronic applications[25–28]. Noted that organic/inorganic structures with micro-/nanoscale could provide the microresonator for the fundamental investigation of light-matter interaction[16], and contribute to the development of integrated photonic devices such as laser sources, optical waveguide, nonlinear optics, and optical switches[29–31]. Among them, the laser only operates within the microresonator, which is formed by the facets of microcrystals with regular shapes[32,33].

However, controlled synthesis of organic microcrystal with regular shape has not been fully realized. Organic micro- and nanostructures fabricated from organic molecules are based on the intermolecular interaction like van der Waals' force, *ca.* 5 kJ/mol. It is different from the strong bonding interaction, such as ionic bonding, *ca.* 200 kJ/mol, within the inorganic crystals. Thus the outer environment including the kinds of solvents, temperature, solution concentration, and surfactants could easily affect the nucleation of organic micro-/nanocrystals[34,35]. These influencing factors are so numerous and sophisticated that the aim of organic micro-/nanostructures with controlled shape is not easy to reach. Despite several groups reporting the synthetic procedure for organic micro-/nanostructures with controlled shape[36–39], the shape-engineering of organic micro/nanocrystals is highly desirable[36].

In this paper, we demonstrate the controlled fabrication of one-dimensional microwires (1D-MWs) and 2D microdisks (2D-MDs) as the different kinds of optical microcavities for laser applications. In our study, the self-assembly of organic π-conjugated molecule 3-[4-(dimethylamino)phenyl]-1-(2-hy-droxyphenyl)prop-2-en-1-one (HDMAC) into 1D-MWs and 2D-MDs have been selectively prepared by modulating the kinetic processes of crystal growth. We realize shape-engineering of HDMAC microcrystals through selectively adhering to the growth [002] crystal plane by hydrogen-bonding interaction with protic solvents molecules. Further, single-particle spectroscopy indeed clarifies that these as-prepared 1D-MWs and 2D-MDs show shape-dependent optical resonator properties: 1D-MWs act as Fabry-Pérot (FP) mode resonators while 2D-MDs function as whispering-gallery-mode (WGM) resonators for laser applications. More importantly, we found that the shape and the size of these self-assembled HDMAC single crystalline microstructures could modulate the behaviors of the laser devices. These easily fabricated organic single-crystalline microcrystals can behave as the optical resonators for laser applications, which contribute to the miniaturization of optics circuits at micro/nanoscale.

Results

The self-assembly of HDMAC microstructures. We firstly simulated the growth shape of HDMAC crystal based on attachment energies using Materials Studio package[40]. From the simulation results, the growth morphology of HDMAC molecules is predicted as 2D disk-like structure, as shown in Fig. 1a. In our experiments, a facile solution drop-drying method was applied to fabricate the microstructures of small organic molecule 3-[4-(dimethylamino)phenyl]-1-(2-hy-droxyphenyl)prop-2-en-1-one (HDMAC). In a typical synthesis, HDMAC was completely dissolved in solvent at room temperature, and then the solution was dropped onto the quartz substrate. With the solvents evaporating, microcrystals were obtained finally. Interestingly, we found that the shape of as-prepared microcrystals depends sensitively on different solvents: protic solvents and aprotic solvents. That is: one-dimensional HDMAC microwires (1D-MWs) were obtained by choosing the protic solvents such as C_2H_5OH, CH_3OH, and *i*-C_3H_7OH; Meanwhile the 2D HDMAC microdisks (2D-MDs) were prepared by choosing the aprotic solvents such as CH_2Cl_2, $CHCl_3$, *n*-C_6H_{14}, and CS_2. Figure 1b shows a typical scanning electron microscopy (SEM) image of the as-prepared HDMAC 1D-MWs with regular shapes. SEM and atomic force microscope (AFM) measurements of these as-prepared 1D-MWs disclosed that the 1D-MWs have the length (l) of 10 ~ 30 μm, the width (w) around 1 μm, and the height (h) around 500 nm (Supplementary Fig. S1a). Meanwhile Figure 1c presents the SEM image of as-prepared HDMAC 2D-MDs, which has regular rectangular shapes and smooth faces. Combined with the AFM measurements together (Supplementary Fig. S1b), these 2D-MDs have the edge width (w_1 or w_2) ranging from 2 μm to 10 μm, and the average height (h) of 600 nm. Based on the above structure-characterizations of these two kinds of the as-prepared microcrystals, it is concluded that the self-assembled 1D-MWs and 2D-MDs could be prepared respectively by just adjusting the kinds of solvents (protic solvents and aprotic solvents) in the process of crystal growth.

More impressively, Figure 1d shows that these as-prepared 1D-MWs exhibit strong red photoluminescence (PL) under the excitation of un-focused UV light (330–380 nm), with typical features of an active optical waveguide, such as brighter PL spots at the two tips and weaker PL from the bodies. This suggests that the 1D-MWs are able to absorb the excitation UV light and propagate the PL along the 1D direction, leading to bright tips when PL exits the 1D-MWs. In sharp contrast, the PL image of 2D-MDs shows bright PL at the four edges of microdisks and little PL from the bodies (Fig. 1e). This indicates that the 2D-MDs can circulate the PL inside its 2D microresonator and possess obvious advantage over 1D-MWs in light-confinement. Significantly, these behaviors of PL images indicate that these self-assembled 1D-MWs and 2D-MDs could simultaneously work as active media of fluorescence emission and optical microresonators with regular shapes[32].

Mechanism for the shape-engineering of HDMAC microcrystals. To investigate the molecular packing mode of HDMAC molecules within 1D-MWs and 2D-MDs, selected area electron diffraction (SAED) and X-ray diffraction (XRD) measurements were carried out. The transmission electron microscopy (TEM) images of individual 1D-MW and 2D-MD are respectively shown in Fig. 2a and 2b. And the insets of Fig. 2a and 2b depict the selected area electron diffraction (SAED) pattern, recorded by directing the

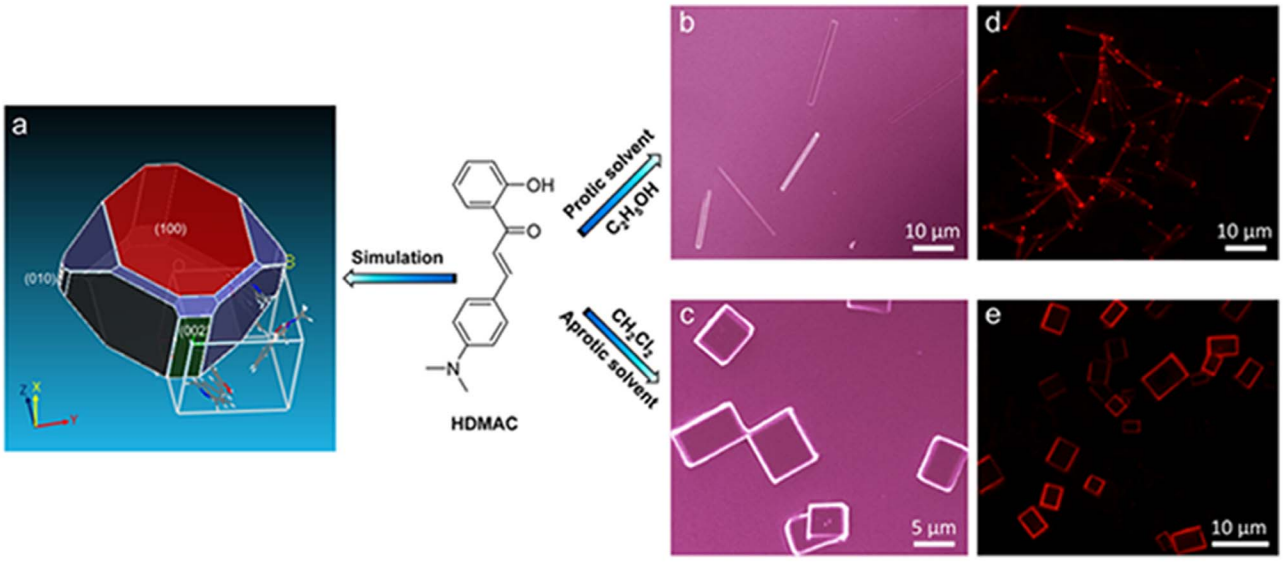

Figure 1 | Self-assembly of one organic molecule HDMAC into 1D microwires and 2D microdisks. (a) The predicted growth morphology of HDMAC molecules based on the attachment energies. (b) and (c) SEM images of as-prepared HDMAC 1D microwires and 2D microdisks, respectively. (d) and (e) Photoluminescence (PL) microscopy images of the as-prepared 1D microwires and 2D microdisks excited with UV band (330–380 nm) from a mercury lamp.

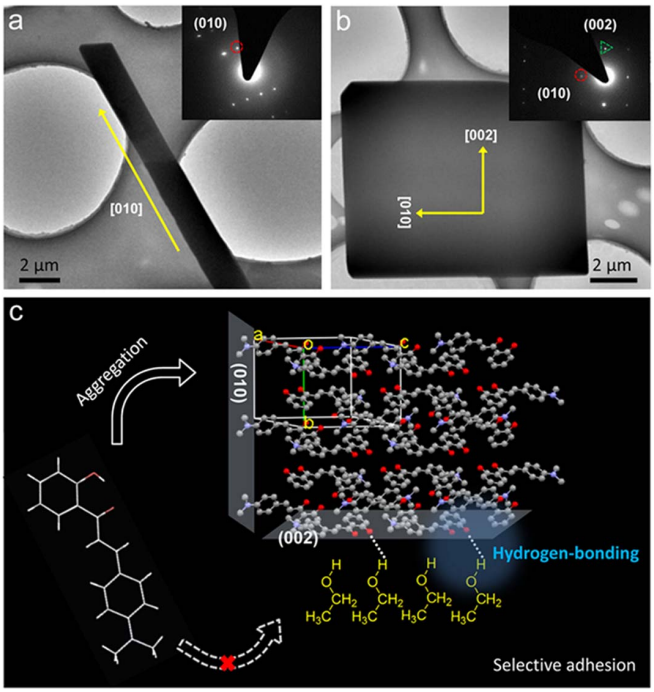

Figure 2 | Selective adhesion to the (002) HDMAC crystal plane via hydrogen-bonding interaction. (a) The TEM image of one typical microwire. Inset: the SAED pattern of this selected microwire. (b) The TEM image of one typical microdisk. Inset: the SAED pattern of this corresponding microdisk. (c) The HDMAC molecular packing mode in microcrystal and schematic depiction for the mechanism of crystal growth.

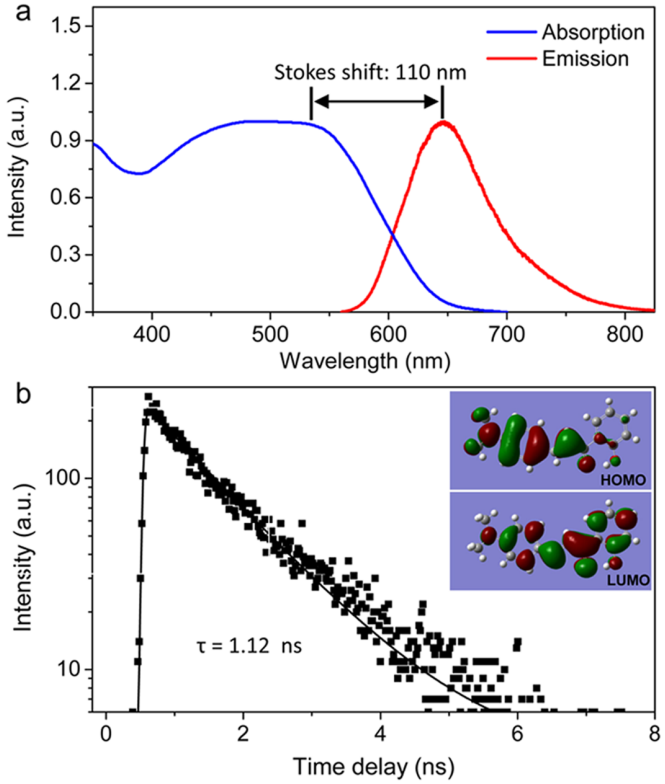

Figure 3 | The photophysical properties of the HDMAC microcrystals. (a) Absorption (blue line) and photoluminescence spectra (red line) of HDMAC microcrystals. (b) Photoluminescence decay, at room temperature, from the microcrystals, showing a lifetime of 1.12 ns. Right inset: The HOMO and the LUMO of HDMAC molecule simulated with DFT calculation.

electron beam perpendicular to the corresponding individual lying microwire and microdisk, respectively. On the basis of the monoclinic single-crystal data of HDMAC, both 1D-MWs and 2D-MDs belong to the cell parameters of a = 12.1194(14) Å, b = 10.2869(8) Å, c = 12.5048(16) Å, $\alpha = \gamma = 90^{\circ}$, β = 115.864(8)°[41]. Further analysis of SAED pattern in the inset of Fig. 2a, the circled SAED spot corresponds to (010) crystal plane with a d-spacing value of 10.3 Å. It indicates that 1D-MWs preferentially grow along the crystal [010] direction. In contrast to the 1D-MW, the 2D-MD shows 2D-growth direction. In the inset of Fig. 2b, the triangled sets of SAED spots are ascribed to reflections from (002) crystal planes with a d-spacing value of 6.3 Å, while the circled set of SAED spots is due to (010) crystal planes with a d-spacing value of 10.2 Å. Additional X-ray diffraction pattern (supplementary Fig. S2) has validated the formation of single-crystalline 1D wires and 2D disks with only a sequence of peaks corresponding to the (100) crystal planes, while other peaks observable in the powder pattern (black curve) are not detected. This indicates the relative abundance of (100) facets on the surfaces of 1D-MWs and 2D-MDs facets. We can conclude that single crystalline 1D-MWs preferentially grow along the [010] direction while single crystalline 2D-MDs grow along the two directions: [010] and [002] crystal directions.

Returning to the predicted growth morphology (Fig. 1a), the corresponding calculated attachment E_{att} (hkl) of various crystal faces (hkl) follows the order: E_{att} (002) ≈ E_{att} (010) > E_{att} (110) ≈ E_{att} (011) > E_{att} (100) (Supplementary Table S1). Correspondingly, [002] and [010] are the two prominent HDMAC crystal growth directions ignoring the solvent-effect. Further insight into the molecular packing mode along these two crystal directions, we can find that the OH-groups of HDMAC molecules are outward-packing on the (002) crystal plane, which will interact with the protic solvent molecules, such as C_2H_5OH, due to the formation of hydrogen-bonding as shown in Fig. 2c. Moreover, the optimized structure of the HDMAC-C_2H_5OH complex indicates that hydrogen-bonding interaction does exist between the HDMAC molecule and the C_2H_5OH molecule (Supplementary Fig. S3). This suggests that the protic molecules selectively "protect" the crystal plane (002) of HDMAC crystal, which impedes the growth of the [002] direction in the process of crystal growth. Therefore, by choosing the protic solvents like C_2H_5OH, the [010] crystal direction becomes the unique growth direction. Thus, the 1D-MDs are the dominated crystal morphology in protic solvents. In sharp contrast, 2D-MDs were obtained in aprotic solvents like CH_2Cl_2. The crystal plane (002) and (010) are both "free" in aprotic solvents. In this case, the directions [010] and [002] are the two prominent growth crystal directions indicated by the attachment energy E_{att} (hkl) order (E_{att} (002) ≈ E_{att} (010)) of various crystal planes. This explains that the obtained microcrystal is similar with the calculated growth morphology of 2D disk-like structure. In a short conclusion, controlled synthetic procedures of HDMAC 1D-MWs and 2D-MDs have been developed by easily choosing different kinds of solvents to control the growth kinetic of morphology growth.

The photophysical properties of HDMAC microstructures. Note that HDMAC belongs to a typical intramolecular charge-transfer (ICT) compound, as indicated by the obvious change of electric-cloud distribution between the Highest Occupied Molecular Orbital (HOMO) and the Lowest Unoccupied Molecular Orbital (LUMO) of the HDMAC molecule by the DFT caculation (right inset of Fig. 3b). Due to the photophysical properties of the ICT excited state, the photoluminescence (PL) emission spectrum (red line in Fig. 3a) of the HDMAC crystals shows the central emission around 650 nm with no fine electronic-phonon coupling structures.

Further analysis of the absorption (blue line in Fig. 3a) and the emission spectra (red line in Fig. 3a), we can find that the HDMAC crystal has a large stokes shift around 110 nm. This large shift contributes to the reduction of self-absorption effect in the optical materials[42]. More importantly, the HDMAC single crystal has excellent optical properties with solid quantum yield Φ of 30 $\pm$ 0.5% and the efficient radiate decay rate k_f = 0.27 $\pm$ 0.1 ns^{-1} according to the equation, $k_f = \Phi/\tau$ (τ = 1.12 $\pm$ 0.03 ns, as shown in Fig. 3b)[43]. These outstanding optical properties hold a promise that the HDMAC could be a candidate active media for the laser action.

1D microwire FP-mode laser microresonator. In order to investigate the optical microresonator effect of these microcrystals, we characterized isolated single-particle spectroscopy using a home-made optical microscope equipped with a 50 × 0.9 NA objective (Supplementary Fig. S4). The second harmonic (λ = 400 nm, pulse width 150 fs) of a 1 KHz Ti:sapphire regenerative amplifier was amplified to a 50 μm diameter spot to uniformly excite the selected isolated microcrystal on a 2D movable table. Spatially resolved PL spectra were collected underneath by using a 3D-movable objective coupled to an optical fiber and detected using a liquid-nitrogen cooled charge-coupled device (CCD). Room temperature lasing oscillator was achieved in the individual 1D-MW by increasing the pump density of the optical excitation. Figure 4a shows the emission spectra at different pump densities obtained from one sample microwire with the length l = 25.9 μm. When the pump density exceeds a threshold E_{th} of 1.05 μJ/cm^2, strong laser emission emerges as a set of sharp peaks around 650 nm. And the full-width-half-maximum (FWHM) of the central resonance peak around 650 nm versus the pump density is plotted (Supplementary Fig. S5). The FWHM has a nearly constant value of about 10 nm at low pump density, and abruptly narrows to the small value of 0.5 nm at high pump density. The abrupt decrease of line-width and the small FWHM value of 0.5 nm comfrim the lasing action within our as-prepared 1D-MWs resonators[3]. And the right inset of Fig. 4a shows the integrated intensities of emission as a function of pump density. The intensity dependence is fitted to power law x^p and p = 0.48 below threshold, assigned to a sublinear regime where bimolecular quenching (exciton-exciton annihilation) dominates[44], and p = 2.41 above the threshold ascribed to superlinear regime are achieved. Moreover, the μ-PL images of the selected 1D-MW were recorded below and above the laser threshold, as shown in the Fig. 4b and 4c, respectively. Further insight into these two images, the μ-PL image below threshold only shows weak PL on the two facets along the length of the microwire. Meanwhile two strong red impressive spots emerge on the two tails of the microwire above the lasing threshold. This indicates that these two facets of microwire function as two reflective planes, which is a characteristic of FP-mode optical microresonator. Thus the emitted PL light forms a standing wave inside this kind of FP-mode microresonator (top inset of Fig. 4d).

To further confirm this FP-mode of 1D-MW laser microresonator, 10 microwires with different lengths were studied (Supplementary Fig. S6). For the PL spectra of FP-type resonance, the mode spacing $\Delta\lambda_m$ (between two adjacent resonance peaks) is given by

$$\Delta\lambda_m = \frac{\lambda^2}{L[n - \lambda(dn/d\lambda)]} \quad (1)$$

where L is the round trip length within one microwire microresonator (a function of the length of microwire: $L = 2l$), λ is the wavelength of light, n is the phase refractive index, and $dn/d\lambda$ is the dispersion relation[3]. A plot of $1/L$ of the microribbons versus the mode spacing $\Delta\lambda_m$ at 650 nm is shown in Fig. 4d. The best-fit line (black line) is clearly linear, which confirms that the microribbon operates as FP-mode resonator along the length rather than the other dimensions of the microribbons. Furthermore, the simulation of two-dimensional (2D) electric field distribution along the cross section of sample microwires confirm that the FP-mode indeed exists along the length direction of the individual 1D-wire (Fig. 4e, and supplementrary Fig. S6e–g). As discussed above, the single 1D-MW provides both a gain medium and a FP-mode resonator for lasing, and so are means with which to realize compact organic photonic lasers.

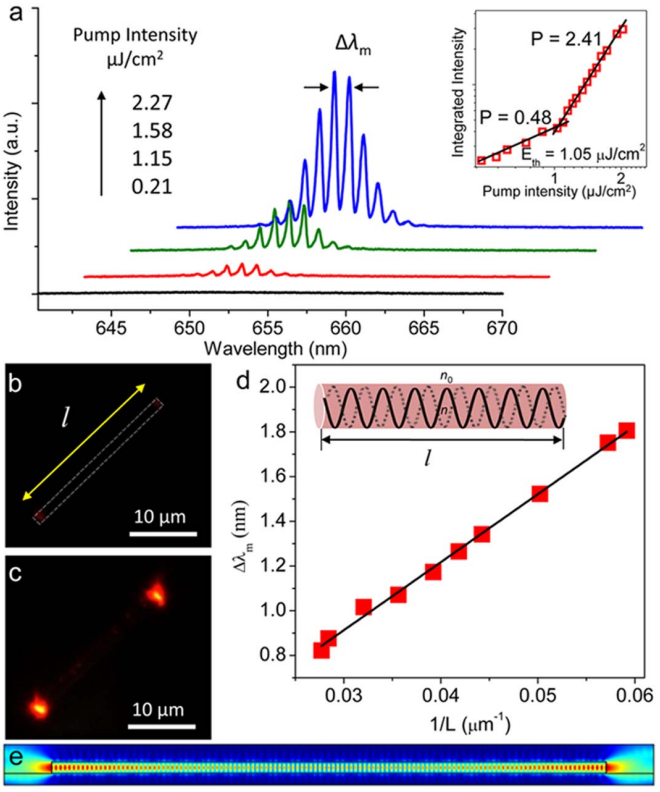

Figure 4 | FP-mode lasing from 1D microwires microresonators. (a) The μ-PL spectra of the individual microwire with the length l = 25.9 μm under different pump pulse energies at room temperature. Right inset: Integrated area emission as a function of pump density. The lasing threshold is identified as the intersection between the sublinear and superlinear regions. (b) and (c) The optical images of the individual 1D-MW below and above the lasing threshold. (d) The mode spacing $\Delta\lambda_m$ at 650 nm versus $1/L$ (L: the length of round trip within microwire microresonator), showing clearly a linear relationship. (e) Simulated 2D normalized electric field (λ = 650 nm, n = 1.80) in the cross section of microwire (l = 25.9 μm, h = 0.50 μm). Red corresponds to the highest field density and blue is the lowest field density.

2D microdisk WGM laser microresonator. Figure 5a shows the dependence of PL spectra from a sample microdisk (w_1 = 4.4 μm and w_2 = 3.8 μm) at different pump densities, with onset lasing at 0.43 μJ/cm^2. The right inset of Fig. 5a shows the integrated area emission as a function of pump density. And the lasing threshold E_{th} = 0.43 μJ/cm^2 is identified as the intersection between the sublinear (p = 0.49) and the superlinear (p = 2.47) regions. As we can observe, single-mode lasing obviously occurs when the pump density exceeds the pump density of 1.2 E_{th}. Moreover, the μ-PL images of the selected 2D-MD were also recorded below and above the laser threshold, as shown in the Fig. 5b and 5c, respectively. Figure 5b shows brighter PL at the four edges of microdisk and weaker PL at the body of 2D-MD, which is a characteristic of 2D WGM optical microresonator. Meanwhile the strong laser emission spots occurs on the four edges of the microdisk when the excitation density exceeds the threshold E_{th} = 0.43 μJ/cm^2, as shown in Fig. 5c.

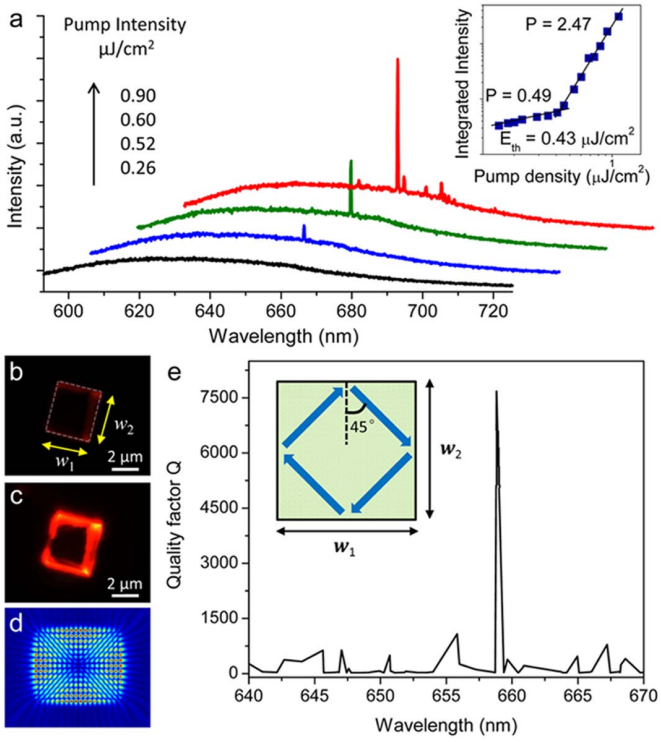

Figure 5 | WGM lasing based on 2D microdisks microresonators. (a) The spectra of the individual rectangular microdisk with edge length w_1 = 4.4 μm and edge length w_2 = 3.8 μm under different pump pulse energies at room temperature. Inset: integrated area emission as a function of pump density. The lasing threshold is identified as the intersection between the sublinear and superlinear regions. (b) and (c) The optical images of the 2D-MP below and above lasing threshold. (d) Simulated 2D normalized electric field (λ = 650 nm, n = 1.80) of microdisk (w_1 = 4.4 μm, w_2 = 3.8 μm). Red corresponds to the highest field density and blue is the lowest field density. (e) The calculated quality factor Q of this microdisk microresonator versus the wavelength of the emission range (from 640 nm to 670 nm). Inset: schematic picture of the light-path of WGM in 2D-MD microresonator.

It indicates that the microdisk can act as the efficient 2D microresonator, in which the light is totally reflected by the four lateral sides of the microdisk.

In order to further confirm the cavity mode in this 2D-MD microresonator, we calculated quality factor (Q) versus the wavelength (λ) of PL, as plotted in Fig. 5e. It should be mentioned here that the Q factor is an important parameter to describe a laser cavity. The calculation results show that there exists only one high-Q mode (~7500) in this sample 2D-MD microresonator. More importantly, it is consistent with the above-observed single-mode lasing within this 2D-MD in the experiment. Meanwhile Figure 5d shows the simulation of 2D electric field distribution corresponding to this corresponding high-Q mode in this microdisk. And this electric distribution result indicates that the high-Q WGM exists in this 2D-MD resonator. As the light circulates inside the microdisk in the form of WG-like route as the inset of Fig. 5e illustrates, the round trip length L within this 2D-MD resonator could be expressed as

$$L = 2\sqrt{w_1^2 + w_2^2} \qquad (2)$$

where L is the round trip length within one microdisk microresonator, w_1 and w_2 are the edge lengths of microdisk as denoted in the inset of Fig. 5e. Based on these experiment results, we can have a conclusion that these self-assembled 2D-MDs exhibit the potential application for miniaturized WGM laser devices.

Size-effect of microstructures on the lasing behavior. To explore the size-effect of resonators on the lasing performance, different sizes of 1D-MWs and 2D-MDs are investigated. In principle, the gain of lasing action is determined by the spatial spectra and the spectral overlap between the resonance of resonator and the gain material[32,45]. The resonance of resonator is regulated by the size of the resonator, which will determine the laser action of these self-assembled microresonators. As we can see from the above results about the lasing spectra of 1D-MWs, the microwires with larger length l has more resonance peaks on the lasing spectra (Supplementary Fig. S6). In the case of the 2D-MDs, Fig. 6a shows the four lasing spectra sequentially from top to bottom, obtained from the four sample 2D-MDs, whose SEM images are shown in Fig. 6b–e respectively. Furthermore, Figure 6f–i demonstrate the simulated electric distribution of these four microdisks. These calculation results all illustrate that the 2D-MDs can act as the efficient WGM optical resonators. For a 2D-MD cavity, the free spectral range, FSR (the spacing between the adjacent resonance peaks), is also given by $(\lambda^2/L)(n\text{-}\lambda(dn/d\lambda))^{-1}$, where L is the round trip length within the 2D-MD resonator (referring to Equation 2), λ is the wavelength of light, n is the phase refractive index, $dn/d\lambda$ is the dispersion relation for the refractive index[3]. As for the same wavelength λ, the value of $\lambda^2(n\text{-}\lambda(dn/d\lambda))^{-1}$ keeps constant even the size of 2D-MDs varies. Thus, a plot of $1/L$ of the 2D-MDs versus the FSR around 650 nm is shown in Fig. 6j. The best-fit line (black line) is clearly linear, which again confirms that the 2D-MDs indeed operate as the 4-WGM resonators. From the experiment, the Q factor could be obtained according to $Q = \lambda/\Delta\lambda$, where λ is the wavelength and $\Delta\lambda$ is the line-width of the lasing peak. Moreover, the determined Q-factor is in the range of 1000 to 7000, which shows linear with the round trip length L within the 2D-MDs microresonators[46]. More significantly, as the size of microdisks varies from the first sample microdisk (w_1 = 4.4 μm, w_2 = 3.8 μm) to the second sample microdisk (w_1 = 8.8 μm, w_2 = 6.8 μm), the lasing performance varies from single-mode lasing behavior to multi-mode lasing behavior. This demonstrates that the size of 2D-MDs could also determine the single-mode lasing behavior or the multimode lasing behavior of these self-assembled 2D laser devices. Note that WGM is consisted of both TE and TM polarized modes. We find that for small-size 2D-disk, such as that in Fig. 5 with edge length w_1 = 4.4 μm and edge length w_2 = 3.8 μm, only TE polarized modes can be supported. In contrast, both TE and TM polarized modes can be supported in large-size 2D-disks. As a matter of fact, occasionally, the lasing spectra of large-size 2D-disks were found to show two different kinds of polarized peaks (TE-polarized mode and TM-polarized mode), which is consistent with the simulation results (Supplementary Fig. S9). As the same with 1D-MWs, 2D-MDs with larger size can also hold more lasing resonance peaks. Furthermore, carefully comparing these four lasing spectra in Fig. 6a, we can find that the central location of PL emission is 653.2 nm, 656.0 nm, 658.2 nm and 663.6 nm, which are obtained from the 2D-MDs of Fig. 6b–e respectively. This phenomenon indicates that the size of 2D-MDs can modulate the central location of lasing wavelength.

Discussion

The optical microcavtity-effects of the as-prepared 1D-MWs and 2D-MDs have been studied to investigate the shape-property relationship. The lasing characteristics of cavities of different shapes and sizes are dependent upon the optical field confinement and the corresponding field density and its overlap with the active medium, the evanescent components existing, the pumping field distribution and the temporal characteristics of the excitation and the resonator. Comparing the laser behaviours of the 1D-MWs in Fig. 4 and the 2D-MDs in Fig. 5, we found that the shape of the resonators actually has the fundamental effect on the laser behaviours including the laser threshold E_{th}, the quality factor Q, and so on. Among these beha-

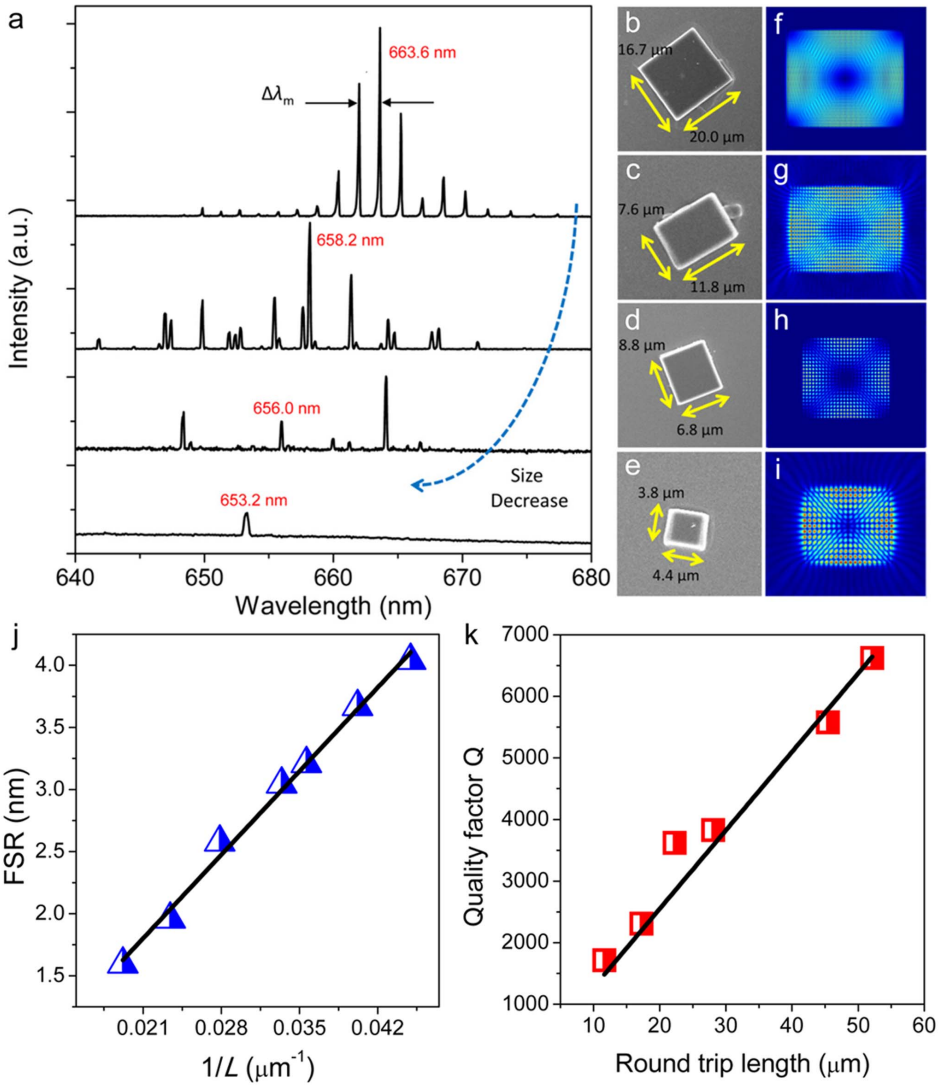

Figure 6 | Modulation of lasing performance (a) The lasing spectra for the four microdisks with different sizes. (b) – (e) The SEM images of the four sample microdisks. The size of these microdisks are denoted with yellow arrow in their individual SEM image. (f) – (i) Simulated 2D normalized electric field (λ = 650 nm, n = 1.80) in the plane of these four corresponding microdisks. Red corresponds to the highest field density and blue is the lowest field density. (j) The FSR at 650 nm versus $1/L$ (L: the length of round trip within 2D-MD resonator), showing clearly a linear relationship. (k) The quality factor Q from the 2D-MDs with different sizes show linear dependence of the round trip length L within 2D-MD microresonators.

viours, the lasing threshold E_{th} is the most important parameter, which determines the minimum energy to operate the laser device. Thus the plots of the laser threshold E_{th} versus the size of 1D-MWs and 2D-MDs are indicated in Fig. 7a and 7b, respectively. It is found that both E_{th} increase with the decreasing size of resonators in these two kinds of microcrystals. Furthermore, for these two geometries, the calculated quality factor Q of microcrystals resonators increases with the increasing size of the corresponding microcrystals, as indicated in Fig. 6k and Fig. 7a. As is known to us, higher Q indicates a lower rate of energy loss relative to the stored energy of the resonator and the oscillations die out more slowly. It also means that high Q resonator can provide the effective platform with good light-confinement for the lasing oscillator.

For nine sample 1D-wires, the laser threshold E_{th} of 1D-MWs ranges from 980 to 2240 nJ/cm^2, as shown in Fig. 7a. And Figure 7b indicates that the E_{th} of thirteen sample 2D-MDs spans from 400 to 890 nJ/cm^2. Based on these experiment results, it is concluded that the 2D-MDs laser resonators have lower threshold E_{th} than that of 1D-MWs laser resonators. According to the COMSOL simulation results (Fig. 4e), it demonstrates that the electromagnetic field distribution both exists within the 1D microwire resonator with a relatively low Q mode (~400) and in the surroundings. Meanwhile, Figure 5d shows that the electromagnetic field entirely distributes within the 2D-MD resonator with a high Q of ~7000. Thus we can conclude that the 2D-disks have better light confinement over the 1D-wires. What's more, that WGM light localization results in great field intensities of the round-trip wavelengths towards the circumference of the 2D-MD resonator, which is also confirmed by the simulated electric energy density results (Supplementary Fig. S10). The 2D-WGM resonators have higher electric energy density than that of 1D-FP resonators. Thus, the better light-confinement and the greater field density would give rise to the lower threshold of 2D-MDs lasers. It should be mentioned here that the high laser threshold of 1D-wires also could be attributed with the low reflectivity of facets and the defects of these microwires. However, from the overall consideration, the shape-engineering of the organic microstructures definitely has the footprint on the laser performance of these miniaturized laser devices.

In summary, one-dimensional (1D) microwires (1D-MWs) and 2D microdisks (2D-MDs) of HDMAC have been selectively prepared

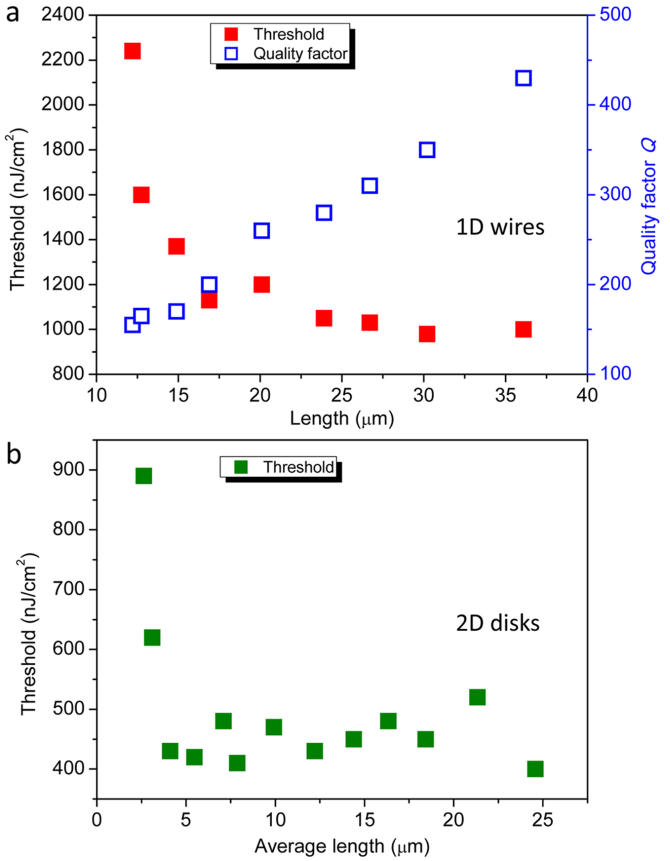

Figure 7 | Shape- and size-dependent laser characteristics. (a) The lasing threshold E_{th} for 1D-MWs microresonators (red squares), and the calculated quality factor Q (blue hollow squares) corresponding to these 1D wires microresonators. (b) The lasing threshold E_{th} for 2D-MDs microresonators (green squares). The average length is define as $(w_1 + w_2)/2$ for 2D-MDs.

by controlling the growth kinetic processes. 1D-MWs and 2D-MDs show strong photoluminescence emission and different optical confinement phenomena. More importantly, pumped by laser, 1D-MWs and 2D-MDs demonstrate different laser actions: single 1D-MW acts as FP-mode optical resonator while 2D-MD functions as WGM optical resonator. The shape and the size of self-assembled microresonators can indeed modulate and affect the performance of laser devices. These easily fabricated organic single-crystalline 1D-MWs and 2D-MDs can act as the laser sources, which offer potential applications as the integrated photonic components at micro/nanoscale.

Methods

Materials. The compound of 3-[4-(dimethylamino)phenyl]-1-(2-hydroxyphenyl)prop-2-en-1-one (HDMAC) was purchased from Sigma-Aldrich and was used without further treatment. The solvent of ethanol (C_2H_5OH, HPLC grade), methanol (CH_3OH, HPLC grade), isopropyl alcohol (i-C_3H_7OH, HPLC grade), dichloromethane (DCM, HPLC grade), chloroform (CH_3Cl, HPLC grade), n-hexane (n-C_6H_{14}, HPLC grade), and carbon disulfide (CS_2, HPLC grade) were purchased from Beijing Chemical Agent Ltd., China.

Preparation of single-crystalline HDMAC microstructures. Microstructures of HDMAC were prepared using a facile drop-drying method. HDMAC was completely dissolved in the aprotic solvents (such as CH_2Cl_2, 2 mM) at room temperature. Then the solution was dropped onto the quartz substrate. Then the solvents evaporated and two dimensional (2D) microdisks were obtained. 1D microwires were obtained by using the protic solvents (such as C_2H_5OH, 2 mM).

Structure characterizations of as-prepared microstructures. TEM images were obtained by a (JEM-1011, JEOL) transmission electron microscopy (TEM). One drop of the solution was dropped on a carbon-coated copper grid, and evaporated. TEM measurement was performed at room temperature at an accelerating voltage of 100 kV. The morphology and the size of microcrystals were also examined by field emission scanning electron microscopy (S-4800, Hitachi,) by dropping on a silicon wafer. The height of microstructures is examined by Atomic force microscopy (AFM, Santa Barbara, CA). The X-ray diffraction (XRD) patterns were measured by a D/max 2400 X-ray diffractometer with Cu Kα radiation (λ = 1.54050 Å) operated in the 2θ range from 5° to 30°, by using the samples on the silicon wafer.

Fluorescence microscopy images. Fluorescence images were recorded using an Olympus research inverted system microscope (FV1000-IX81, Tokyo, Japan) equipped with a charge couple device (CCD, Olympus DP71, Tokyo, Japan) camera. The excitation source is a Xenon lamp equipped with a band-pass filter (330–380 nm for UV-light, 460–490 nm for blue plight). The samples were prepared by placing a drop of solution onto a cleaned quartz slide.

Single-particle spectroscopy. Single microcrystal was investigated at room temperature in air by a home-made optical microscopy equipped with a 50 × 0.9 NA excitation objective. The second harmonic (400 nm, 150 fs, 1 kHz) of a regenerative amplifier (Spitfire, Spectra Physics) seeded with a mode-locked Ti:sapphire laser (Tsunami, Spectra Physics) was amplified to a 50-μm-diameter spot to excite the selected individual microcrystal. Then PL spectra were collected underneath by using a 50 × 0.9 NA objective that was mounted a 3D movable stage. A 420-nm long-wave pass dielectric filter was used to block any scattered excitation light. Finally the collected PL was coupled to an optical fiber and detected using a liquid-nitrogen-cooled CCD (SPEC-10-400B/LbN, Roper Scientific) attached to a polychromator (Spectropro-550i, Acton). The spectral resolution is 0.1 nm.

Density functional theory calculation. The Highest Occupied Molecular Orbital (HOMO) and the Lowest Unoccupied Molecular Orbital (LUMO) of HDMAC molecule were simulated with DFT calculation at the B3LYP/6-311G(d,p) level by Gauss 09 package.

Simulation of electric field distribution. We calculated the electric field distribution of our HDMAC 1D microwires microresonator and 2D microdisks microresonator by using a finite element (FE) method (COMSOL). The microstructures are on the quartz substrate (n_{quatz} = 1.45). And the refractive index (n_{HDMAC}) of HDMAC microcrystal is regarded as 1.8, which corresponds to the value at 650 nm.

1. Huang, M. H. *et al.* Room-temperature ultraviolet nanowire nanolasers. *Science* **292**, 1897–1899 (2001).
2. Johnson, J. C. *et al.* Single gallium nitride nanowire lasers. *Nat. Mater.* **1**, 106–110 (2002).
3. Duan, X., Huang, Y., Agarwal, R. & Lieber, C. M. Single-nanowire electrically driven lasers. *Nature* **421**, 241–245 (2003).
4. Tamboli, A. C. *et al.* Room-temperature continuous-wave lasing in GaN/InGaN microdisks. *Nat. Photon.* **1**, 61–64 (2007).
5. O'Carroll, D., Lieberwirth, I. & Redmond, G. Microcavity effects and optically pumped lasing in single conjugated polymer nanowires. *Nat. Nanotechnol.* **2**, 180–184 (2007).
6. Ishai, M. B. & Patolsky, F. Shape- and dimension-controlled single-crystalline silicon and SiGe nanotubes: toward nanofluidic FET devices. *J. Am. Chem. Soc.* **131**, 3679–3689 (2009).
7. Piccione, B., Cho, C. H., van Vugt, L. K. & Agarwal, R. All-optical active switching in individual semiconductor nanowires. *Nat. Nanotechnol.* **7**, 640–645 (2012).
8. Saxena, D. *et al.* Optically pumped room-temperature GaAs nanowire lasers. *Nat. Photon.* **7**, 963–968 (2013).
9. Yu, J. *et al.* Confinement of pyridinium hemicyanine dyewithin an anionic metal-organic framework for two-photon-pumped lasing. *Nat. Commun.* **4**, 2719 (2013).
10. Jin, R. *et al.* Photoinduced conversion of silver nanospheres to nanoprisms. *Science* **294**, 1901–1903 (2001).
11. Fu, H. B. & Yao, J. N. Size effects on the optical Properties of organic nanoparticles. *J. Am. Chem. Soc.* **123**, 1434–1439 (2001).
12. Richter, R. *et al.* Size and shape dependent photoluminescence and excited state decay rates of diamondoids. *PCCP* **16**, 3070–3076 (2014).
13. Aslam, F. & von Ferber, C. Shape dependent properties of CdSe nanostructures. *Chem. Phys.* **362**, 114–119 (2009).
14. Ray, P. C. *et al.* Size and shape dependent second order nonlinear optical properties of nanomaterials and their application in biological and chemical sensing. *Chem. Rev.* **110**, 5332–5365 (2010).
15. Zhang, H., Zhang, X., Sun, X. & Ma, Y. Shape-controlled synthesis of nanocarbons through direct conversion of carbon dioxide. *Sci. Rep.* **3**, 3534–3541 (2013).
16. Wang, X. D. *et al.* Exciton-polaritons with size-tunable coupling strengths in self-assembled organic microresonators. *ACS Photonics*, **1**, 413–420 (2014).
17. Zhang, H. *et al.* Shape-controlled synthesis of Pd nanocrystals and their catalytic applications. *Acc. Chem. Res.*, **46**, 1783–1794 (2013).
18. Xia, X., Zeng, J., Oetjen, L. K., Li, Q. & Xia, Y. Quantitative analysis of the role played by poly(vinylpyrrolidone) in seed-mediated growth of Ag nanocrystals. *J. Am. Chem. Soc.* **134**, 1793–1801 (2012).

19. Chen, R., Ling, B., Sun, X. W. & Sun, H. D. Room temperature excitonic whispering gallery mode lasing from high-quality hexagonal ZnO microdisks. *Adv. Mater.* **23**, 2199–2204 (2011).
20. Orendorff, C. J., Sau, T. K. & Murphy, C. J. Shape-dependent plasmon-resonant gold nanoparticles. *Small* **2**, 636–639 (2006).
21. Nehl, C. L. & Hafner, J. H. Shape-dependent plasmon resonances of gold nanoparticles. *J. Mater. Chem.* **18**, 2415 (2008).
22. Senyuk, B. *et al.* Shape-dependent oriented trapping and scaffolding of plasmonic nanoparticles by topological defects for self-assembly of colloidal dimers in liquid crystals. *Nano letters* **12**, 955–963 (2012).
23. Narayanan, R. & El-Sayed, M. A. Shape-dependent catalytic activity of platinum nanoparticles in colloidal solution. *Nano letters* **4**, 1343–1348 (2004).
24. Clark, J. & Lanzani, G. Organic photonics for communications. *Nat. Photon.* **4**, 438–446 (2010).
25. Takazawa, K., Inoue, J.-i., Mitsuishi, K. & Takamasu, T. Fraction of a millimeter propagation of exciton polaritons in photoexcited nanofibers of organic dye. *Phys. Rev. Lett.* **105**, 067401 (2010).
26. Briseno, A. L. *et al.* Patterning organic single-crystal transistor arrays. *Nature* **444**, 913–917 (2006).
27. Chandrasekhar, N. & Chandrasekar, R. Reversibly shape-shifting organic optical waveguides: formation of organic nanorings, nanotubes, and nanosheets. *Angew. Chem. Int. Ed.* **51**, 3556–3561 (2012).
28. Sundar, V. C. *et al.* Elastomeric transistor stamps: reversible probing of charge transport in organic crystals. *Science* **303**, 1644–1646 (2004).
29. Dong, H. *et al.* Single-crystalline hexagonal ZnO microtube optical resonators. *J. Mater. Chem.* **20**, 5510–5515 (2010).
30. Dong, H. *et al.* Whispering gallery modes in indium oxide hexagonal microcavities. *Appl. Phys. Lett.* **94**, 173115 (2009).
31. Riziotisa, C., Sono, T. J., Mailisc, S. & Eason, R. W. Enhanced second harmonic generation in lithium niobate hexagonal micro-resonator via total internal reflection quasi-phase-matching. *Proc. of SPIE* **8964**, 89641Q (2014).
32. Wang, X. D. *et al.* Whispering-gallery-mode microlaser based on self-assembled organic single-crystalline hexagonal microdisks. *Angew. Chem. Int. Ed.* **53**, 5863–5867 (2014).
33. Gargas, D. J. *et al.* Whispering gallery mode lasing from zinc oxide hexagonal nanodisks. *ACS Nano* **4**, 3270–3276 (2010).
34. Kang, L. *et al.* Colloid chemical reaction route to the preparation of nearly monodispersed perylene nanoparticles: size-tunable synthesis and three-dimensional self-organization. *J. Am. Chem. Soc.* **129**, 7305–7312 (2007).
35. Lei, Y., Liao, Q., Fu, H. & Yao, J. Phase- and shape-controlled synthesis of single crystalline perylene nanosheets and its optical properties. *J. Phys. Chem. C* **113**, 10038–10043 (2009).
36. Kang, L. *et al.* Controlled morphogenesis of organic polyhedral nanocrystals from cubes, cubooctahedrons, to octahedrons by manipulating the growth kinetics. *J. Am. Chem. Soc.* **133**, 1895–1901 (2011).
37. Zhang, X. J. *et al.* Single-crystal nanoribbons, nanotubes, and nanowires from intramolecular charge-transfer organic molecules. *J. Am. Chem. Soc.* **129**, 3527–3532 (2007).
38. Jonkheijm, P., van der Schoot, P., Schenning, A. P. & Meijer, E. W. Probing the solvent-assisted nucleation pathway in chemical self-assembly. *Science* **313**, 80–83 (2006).
39. Liu, H. Y. *et al.* Self-assembly of octachloroperylene diimide into 1D rods and 2D plates by manipulating the growth kinetics for waveguide applications. *Chem. Commun.* **50**, 4620–4623 (2014).
40. Winn, D. & Doherty, M. F. Modeling crystal shapes of organic materials grown from solution. *AIChE J.* **46**, 1348–1367 (2000).
41. Liu, Z. *et al.* 2′-Hydroxy-4″-dimethylamino-chalcone. *Acta Cryst. C* **58**, 445–446 (2002).
42. Xu, Z. *et al.* Low-threshold nanolasers based on slabnanocrystals of H-aggregated organic semiconductors. *Adv. Mater.* **24**, OP216–220 (2012).
43. Lkowicz, J. R. *Principles of fluorescence spectroscopy* (Springer, Berlin-Heidelberg, 2006).
44. Kéna-Cohen, S. & Forrest, S. R. Room-temperature polariton lasing in an organic single-crystal microresonator. *Nat. Photon.* **4**, 371–375 (2010).
45. Chen, R., Van Duong, T. & Sun, H. D. Single mode lasing from hybrid hemispherical microresonators. *Sci. Rep.* **2**, 244–249 (2012).
46. Chen, R., Ta, V. D. & Sun, H. Bending-induced bidirectional tuning of whispering gallery mode lasing from flexible polymer fibers. *ACS Photonics*, **1**, 11–16 (2014).

Author contributions

H.F. proposed and guided the overall project. X.W. and X.L. performed all experiments. X.W., Q.L., H.L. and Z.X. discussed and analyzed the results. All authors substantially contributed to the manuscript.

Additional information

Supplementary information accompanies this paper at http://www.nature.com/scientificreports

Competing financial interests: The authors declare no competing financial interests.

How to cite this article: Wang, X. *et al.* Shape-Engineering of Self-Assembled Organic Single Microcrystal as Optical Microresonator for laser Applications. *Sci. Rep.* **4**, 7011; DOI:10.1038/srep07011 (2014).